Chapter 3

Synthesis and Characterization of $Pd_{4-x}Fe_x/C$ (x = 1-3) and $Pd_3Fe_{0.5}Cu_{0.5}/C$ Nanoparticles: Robust Non-Platinum Electrocatalysts for Enhanced Oxygen Reduction Reaction

Outline

The highly efficient and eco-friendly properties of the fuel cell (FC) make it a promising source of alternative clean energy to meet increasing energy demand. Thus, FC is likely to receive extensive commercial use in the field of transportation, portable power generation etc. thereby solving the global needs of energy demand and clean environment. Owing to its high power density, simplicity, low working temperature as well as quick start-up, the proton exchange membrane fuel cell (PEMFC) has been actively pursued among the existing FCs. The catalyst coating at the cathode in PEMFCs is one of the major limitations for the energy conversion efficiency [1,2]. The oxygen reduction reaction (ORR) at the cathode is somewhat lethargic as compared to that of the oxidation reaction which takes place at the anode. Therefore, significant efforts have been made in developing highly active ORR electrocatalysts. Although Pt or its alloy is regarded as the most effective ORR electrocatalysts, the high price, inferior durability, and the low availability of Pt restrain the mass production and viable commercialization of the FC [1]. Considerable effort has been given to overcome this issue by designing Pt-free or low-Pt electrocatalysts [1]. Recent development indicates that Pd alloying with 1st row transition metals, (M = Fe, Cu, Ni, Co etc.) which form bimetallic or trimetallic alloy [3–12], display substantial enhancement in catalytic performance for both fuel oxidation and ORR. Especially, the impressive enhancement in ORR activity is achieved by constraining the lattice parameter or Pd-Pd interatomic distance, changing the charge distribution and preserving more active sites due to synergistic interaction in bimetallic or trimetallic alloys [13]. Adzic and coworkers showed that alloying Pd with Fe remarkably decreases the lattice constant of Pd, by this means altering the d-band centre and weakened the Pd-O binding by 0.10 V, which as a result offering superior activity towards ORR [14,15]. Recent progresses show that fabrication of ternary alloy or intermetallic in achieving novel structural and electronic properties of Pd-based nanoparticles (NPs) which in turn boost the ORR performance [16-20].

Chapter 3: Synthesis and Characterization of $Pd_{4-x}Fe_x$/C (x = 1-3) and $Pd_3Fe_{0.5}Cu_{0.5}$/C Nanoparticles: Robust Non-Platinum Electrocatalysts for Enhanced Oxygen Reduction Reaction

In this Chapter 3, we have discussed synthesis of different compositions of $Pd_{4-x}Fe_x$/C NPs (x = 1, 2 and 3) and $Pd_3Fe_{0.5}Cu_{0.5}$/C NPs, via a solvothermal route without adding any surfactant. The synthesized NPs were characterized by different analytical and spectroscopic techniques, for instance, XRD, ICP-OES, TGA, EDX, BET surface area, TEM and XPS. The catalytic activities were evaluated towards ORR in both basic and acidic media. Furthermore, we have also investigated how the incorporation of small amount of Cu on optimized composition of Pd_3Fe/C NPs improve the electrocatalytic ORR activity in all respects as compared to that of the standard Pd/C, Pt/C and other compositions of PdFe/C nanocatalyst. The experimental procedures for the synthesis, characterization techniques and catalytic activity were described in the Chapter 2.

3.1. Results and Discussion

3.1.1. Characterization of the Synthesized $Pd_{4-x}Fe_x$/C NPs (x = 1, 2 and 3) and $Pd_3Fe_{0.5}Cu_{0.5}$/C NPs

The compositions of as prepared NPs are determined by EDS and ICP-OES analyses. The EDS analysis of $Pd_3Fe_{0.5}Cu_{0.5}$/C shows that only Pd, Fe, Cu and C are present in the EDS pattern with ~22 wt% loading of metals on carbon matrix. The corresponding EDS elemental maps show that homogeneous dispersion of metals on the carbon (Figure 3.1). The Pd, Fe and Cu atomic ratio are *ca.* 74.81%, 14.56% and 10.61%, which corroborate well with ICP-OES analyses. EDS and ICP-OES results suggest that high uniformity in the surface and bulk composition of $Pd_3Fe_{0.5}Cu_{0.5}$/C NPs.

Moreover, the total metal loading of NPs is calculated by means of TGA analysis in an air environment. The TGA profile (Figure 3.2) displays a sudden weight loss of the sample at about ~350 °C which is due to the oxidation of carbon to carbon dioxide in the sufficient oxidative environment. The residue obtained after burning of all the carbonaceous materials gives information about the loading of the total metal content. The loading of the metal obtained is ~22% in the case of the $Pd_3Fe_{0.5}Cu_{0.5}$/C.

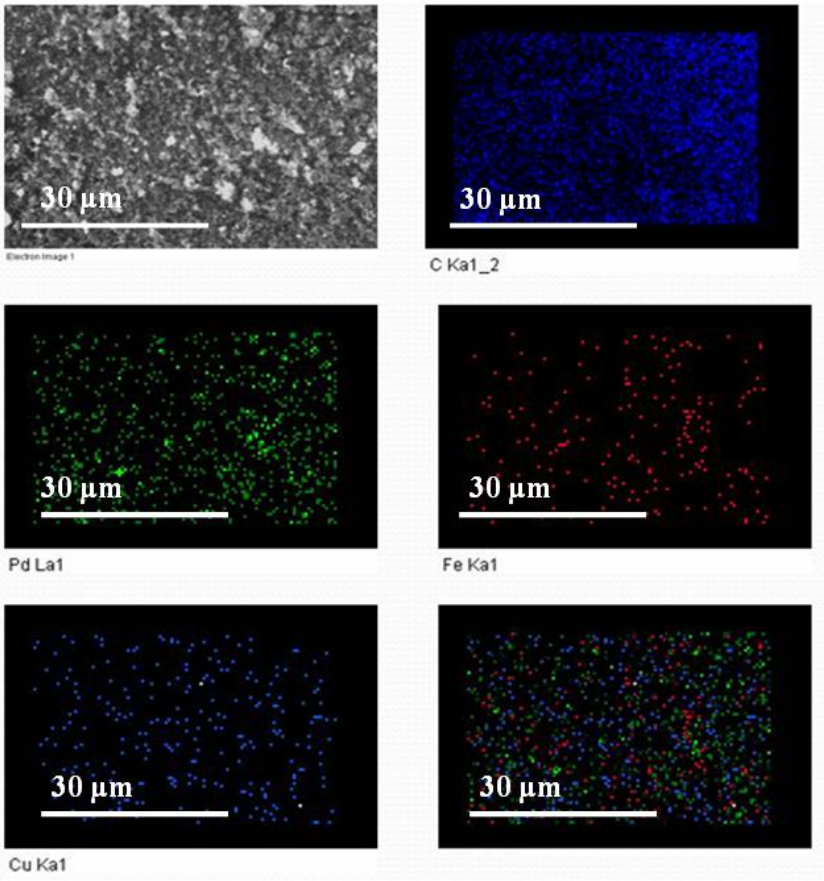

Figure 3.1: EDS elemental mapping of $Pd_3Fe_{0.5}Cu_{0.5}$/C NPs.

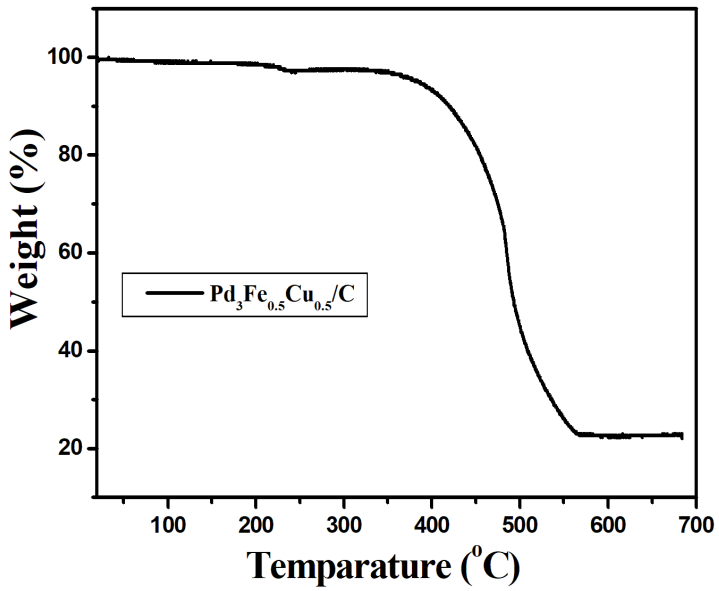

Figure 3.2: TGA profile of $Pd_3Fe_{0.5}Cu_{0.5}$/C NPs in air atmosphere.

The powder XRD patterns of $Pd_3Fe_{0.5}Cu_{0.5}$/C, Pd_3Fe/C, PdFe/C, and $PdFe_3$/C (Figure 3.3a) show mainly characteristic peaks of face centred cubic (fcc) crystalline Pd signifying multiphase disordered structure. The diffraction peaks centred at ~40°, ~47°, and ~68° correspond to the (111), (200), and (220) reflections, respectively. These peaks are slightly shifted to higher angles relative to the pure Pd (JCPDS no. 87-0641) indicating the formation of alloyed NPs [21]. A broad peak observed at around ~25° is ascribed to the (002) reflection of a hexagonal structure in Vulcan XC-72R carbon. No characteristic peak of copper, iron, copper oxide or iron oxides are observed in the XRD pattern of $Pd_3Fe_{0.5}Cu_{0.5}$/C and Pd_3Fe/C. This signifies that Cu and Fe are well incorporated in the fcc lattice of Pd to form a single-phase alloy, or the existence of highly dispersed Cu and Fe species [22]. However, in case of PdFe/C and $PdFe_3$/C with the increase of Fe content, minor peaks are observed in the XRD patterns at 30.1°, 35.5°, 57.2°, and 62.8° which can be assigned to Fe_3O_4 phases (JCPDS no. 19-0629). From Bragg's law ($\lambda = 2d \sin\theta$, where '*d*' is the interplanar spacing between planes in a crystal) and the interplanar spacing equation for a particular cubic crystal (*fcc*, 111) of unit cell parameter '*a*' ($1/d^2 = (h^2 + k^2 + l^2)/a^2$ yields the equation $a = \lambda/2\ ((h^2 + k^2 + l^2)^{1/2}/\sin\theta)$,[23] from which '*a*' values of 0.3910 ($PdFe_3$/C), 0.3906 (PdFe/C), 0.39161 (Pd_3Fe/C) and 0.38918 nm ($Pd_3Fe_{0.5}Cu_{0.5}$/C) are calculated. The calculated 'd' values of 0.2261 (Pd_3Fe/C) and 0.2246 nm ($Pd_3Fe_{0.5}Cu_{0.5}$/C) agrees well with the spacing between planes observed using HR-TEM (See Figure 3.4 h). These values are rather smaller than those for bulk Pd (JCPDS no. 87-0641, a = 0.3961 nm, d = 0.228 nm) and larger than bulk Fe (JCPDS no. 88-2324, a = 0.343 nm, d = 0.198 nm), and bulk Cu (JCPDS no. 85-1326, a = 0.361 nm, d = 0.208 nm) indicating the formation of PdFe bimetallic and PdFeCu trimetallic alloys. The relatively smaller values of '*a*' and *'d'* for $Pd_3Fe_{0.5}Cu_{0.5}$/C, as compared to the other PdFe alloys also implies effective lattice contraction. The Figure 3.3(b) shows the N_2 adsorption-desorption isotherm of $Pd_3Fe_{0.5}Cu_{0.5}$/C, these carbon supported NPs exhibits a high BET specific surface area of 69.8 m^2/g and a large pore volume of 0.104 cc/g.

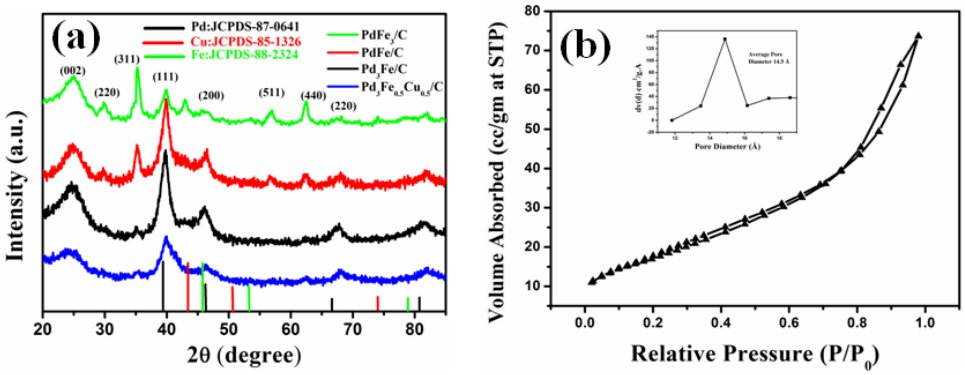

Figure 3.3: (a) XRD patterns of the $Pd_3Fe_{0.5}Cu_{0.5}$/C, Pd_3Fe/C, PdFe/C, and $PdFe_3$/C electrocatalysts, and (b) N_2 adsorption-desorption isotherm of $Pd_3Fe_{0.5}Cu_{0.5}$/C. Inset of (b) shows the corresponding pore size distribution.

The shape and microstructure of $Pd_3Fe_{0.5}Cu_{0.5}$/C NPs are further studied by TEM and HR-TEM and presented in Figure 3.4. From the TEM images (Figure 3.4 a-c) it could be observed that many nearly-spherical $Pd_3Fe_{0.5}Cu_{0.5}$ NPs of dark contrast are highly dispersed on the larger particles of Vulcan XC-72 R carbon of lighter contrast. The average particle-size of $Pd_3Fe_{0.5}Cu_{0.5}$ NPs is estimated to be about ~ 6-7 nm (inset in Figure 3.4a). The NPs exhibit various crystal defects on their surfaces, for instance vacancy, dislocation and low-coordinate atomic steps, as manifested in HR-TEM images (Figure 3.4 d,e). Because of these coordinative unsaturation the NPs can serve as catalytic sites, [24,25] successfully enhancing the electrocatalytic activity [26,27].

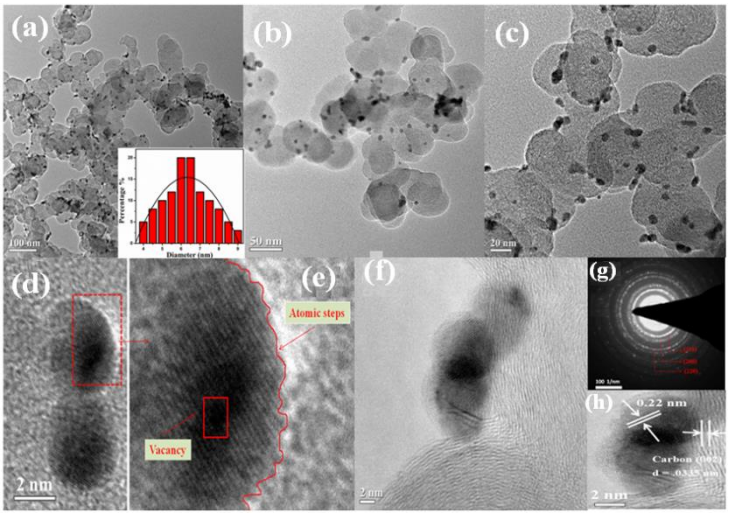

Figure 3. 4: Typical (a) low, (b,c) medium, and (d-f,h) high resolution-TEM images of $Pd_3Fe_{0.5}Cu_{0.5}$/C, (g) corresponding SAED pattern, (e) is magnified HR-TEM image taken from (d), marked by the rectangle.

Furthermore, as shown in Figure 3.4f, $Pd_3Fe_{0.5}Cu_{0.5}$ NPs are half-embedded in the carbon matrix which generate rich interface that favors high electrocatalytic activity. The concentric circles with well-defined crystalline facets in the SAED pattern (Figure 3.4g) infer high crystallinity of the $Pd_3Fe_{0.5}Cu_{0.5}$/C NPs. The comprehensible d-spacings ~0.22 nm (Figure 3.4h) can be observed in the lattice fringes of $Pd_3Fe_{0.5}Cu_{0.5}$/C NPs, close to the fcc Pd (111) facets, signifying high crystallization. The distribution of the constituent elements is determined by elemental mapping analyses. The Figure 3.1 clearly shows that Pd, Cu, Fe and C are homogeneously distributed. This observation further provides the proof of the formation of alloy structure of $Pd_3Fe_{0.5}Cu_{0.5}$/C. The detailed morphological characterization of Pd_3Fe/C is also performed by TEM and HR-TEM analyses and presented in Figure 3.5 As estimated, the Pd_3Fe/C alloy shows an analogous morphology and surface/interface structure with that of $Pd_3Fe_{0.5}Cu_{0.5}$/C NPs. Based on the above discussion, we could deduce that spherical and nearly homogeneous Pd-based NPs can be effectively synthesized by simple solvothermal method without using any harmful structure directing solvents and surfactants.

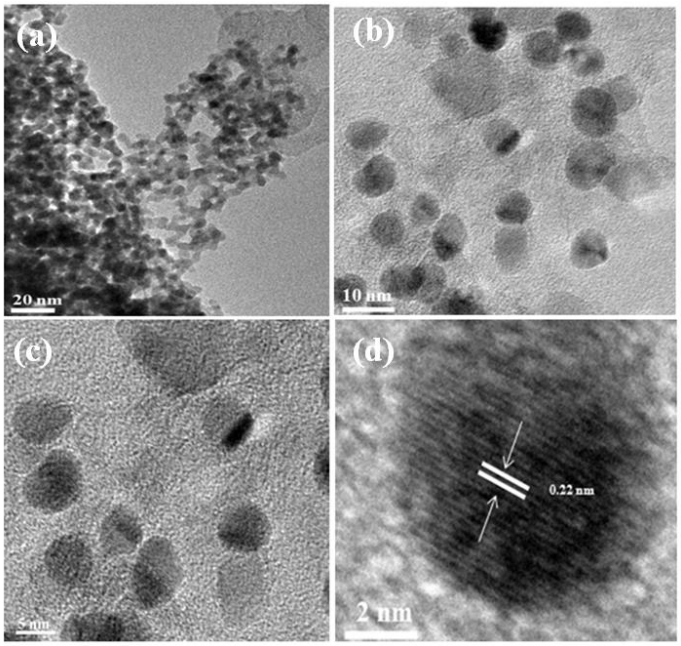

Figure 3.5: TEM and HR-TEM images of Pd_3Fe/C NPs.

XPS is extensively performed to elucidate the chemical composition of NPs. Figure 3.6 a-d illustrates the XP spectra of C 1s, Pd 3d, Fe 2p and Cu 2p regions of $Pd_3Fe_{0.5}Cu_{0.5}$/C. The C 1s core-level XP spectrum (Figure. 3.6a) of $Pd_3Fe_{0.5}Cu_{0.5}$/C is

slightly asymmetric and hence, can be deconvoluted into three different peaks viz., a prominent peak at 284.6 eV along with two small peaks at 285.9 and 289.8 eV, consistent to form –C=C−, −C−O−, and O=C−O− bonds, respectively [28,29]. It can also be seen from Figure 3.6a that the small integration areas for −C−O− and O=C−O− peaks specify low O content as compared to that of the −C=C− bond. This trace amount of O element generally arises from the adsorbed air on the catalyst surface during storage and sample analysis. The core-level Pd 3d spectrum displays a doublet signal with binding energies of 335.7 and 341.0 eV for Pd $3d_{5/2}$ and Pd $3d_{3/2}$, respectively, corresponding to the Pd signal [30]. Additionally, small doublets observed around 336.9 and 342.5 eV could be indexed to the Pd $3d_{5/2}$ and Pd $3d_{3/2}$ peaks of PdO (Figure 3.6b) [31]. The Figure 3.6c shows the Fe 2p core-level spectrum for the NPs. Two prominent peaks at 711.1 and 724.9 eV corresponds to the Fe $2p_{3/2}$ and Fe $2p_{1/2}$ core-level energies of iron oxide. The binding energy positions clearly indicates that the iron oxide in the NPs is in the form of magnetite (Fe_3O_4) [32,33]. The corresponding values for maghemite (γ-Fe_2O_3) occur at slightly lower binding energy at 710.0 and 723.6 eV, respectively [34–36]. The emerging photoelectron peaks of Fe^{3+} may be attributed to the easy oxidation of zero valent iron (ZVI) in air, which could result in a layer of iron oxide around the ZVI NPs. No peak of metallic Fe (708.0 eV) is observed signifying Fe oxides to be the major class on the $Pd_3Fe_{0.5}Cu_{0.5}$ alloy surface. The formation of Fe oxides can be attributed to the oxidation of Fe atoms on the catalyst surface during drying and sampling. The peaks observed at 932.0 and 951.8 eV from the Cu $2p_{3/2}$ and Cu $2p_{1/2}$ spin−orbit doublets, respectively, correspond to a metallic copper (Figure 3.6d), which is consistent with Cu NPs [37,38]. The binding energy peaks of the three constituent elements Pd $3d_{5/2}$, Fe $2p_{3/2}$ and Cu $2p_{3/2}$ are shifted as compared to that of the standard literature values. For Pd, a positive shift of ~0.50 eV, while, for Fe and Cu negative shifts of ~0.67 eV and ~0.50 eV, respectively, are observed in the binding energy values. The strong charge transfer between Pd, Fe and Cu is responsible for the alloy formation [39–42].

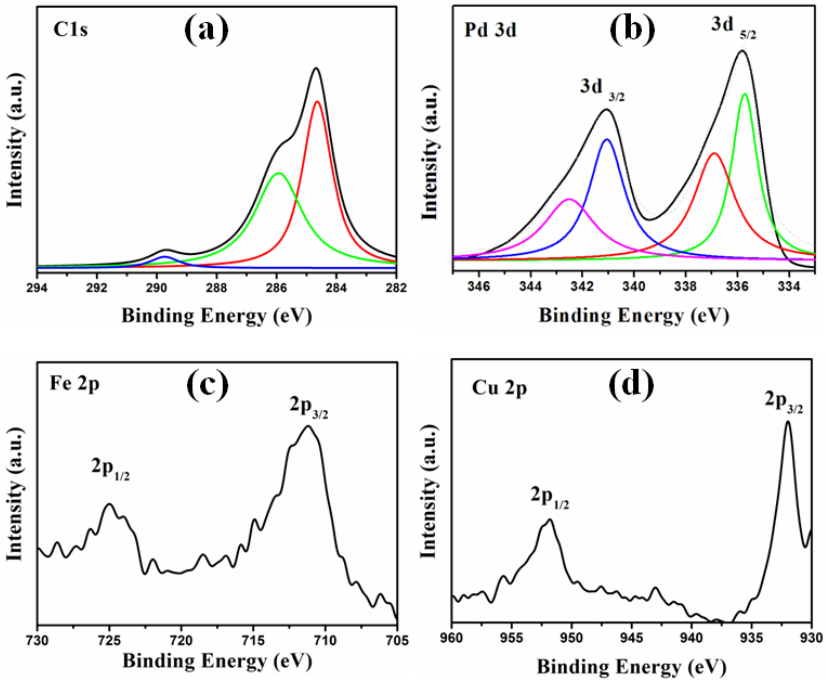

Figure 3.6: (a) C 1s, (b) Pd 3d, (c) Fe 2p, and (d) Cu 2p XP spectra of $Pd_3Fe_{0.5}Cu_{0.5}/C$.

For the bimetallic Pd_3Fe/C, the clear shift of binding energy for both Pd and Fe peaks in comparison to the standard monometallic counterparts is a strong evidence of efficient PdFe nanoalloy formation (Figure 3.7).

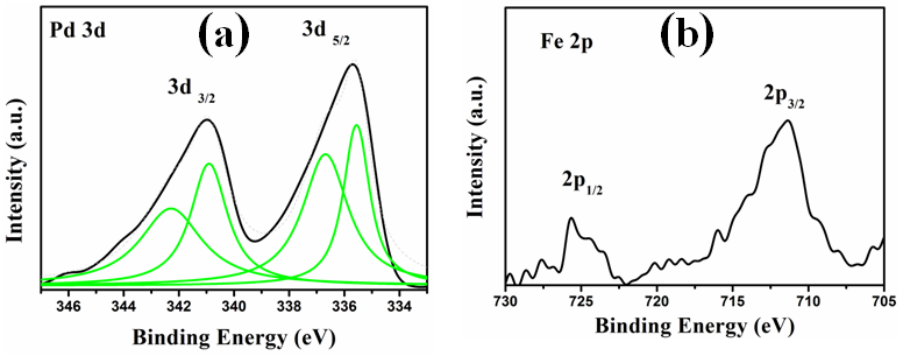

Figure 3.7: The core-level XP spectrum of (a) Pd 3d and (b) Fe 2p of Pd_3Fe/C NPs.

3.1.2. Electrocatalytic Activity

The electrocatalytic behavior of the binary $PdFe_3/C$, PdFe/C, and Pd_3Fe/C, and ternary $Pd_3Fe_{0.5}Cu_{0.5}/C$ modified glassy carbon electrode (GCE) are measured in N_2- and O_2-saturated 0.1 M KOH, as shown in Figure 3.8 - 3.11. Figure 3.8a shows the CV plots of $Pd_3Fe_{0.5}Cu_{0.5}/C$ NPs in N_2- and O_2-saturated 0.1 M KOH solution. A strong and well-defined reduction peak is observed in O_2-saturated 0.1 M KOH solution

whereas no such characteristic reduction peak is observed in N_2-saturated electrolyte, signifying that the synthesized $Pd_3Fe_{0.5}Cu_{0.5}$/C NPs has a good electrocatalytic activity towards ORR. Moreover, to determine the kinetics of ORR for $Pd_3Fe_{0.5}Cu_{0.5}$/C NPs, rotating disk electrode (RDE) measurement is performed in O_2-saturated 0.1 M KOH solution at a rotating rate of 400, 900, 1600, 2500 and 3600 rpm as shown in Figure 3.8b. Based on the ORR polarization curves, the number of electrons (n) transferred during ORR can be evaluated using the following Koutecky−Levich (K−L) equation [43].

$$1/j = 1/j_k + 1/B\,\omega^{0.5}$$

$$B = 0.62\,nF(Do_2)^{2/3}\nu^{-1/6}\,Co_2$$

Where, j = current density, j_k = kinetic current density, ω = rotating rate of the electrode, B = value of slope obtained from the K−L plots, F = Faraday constant (96485 C mol^{-1}), Do_2 = diffusion coefficient of O_2 in 0.1 M KOH solution, ν = kinetic viscosity (0.01 $cm^2\ s^{-1}$), Co_2 = bulk concentration of O_2 (1.2×10^{-6} mol cm^{-3}), and n = the number of electrons transferred in the ORR process.

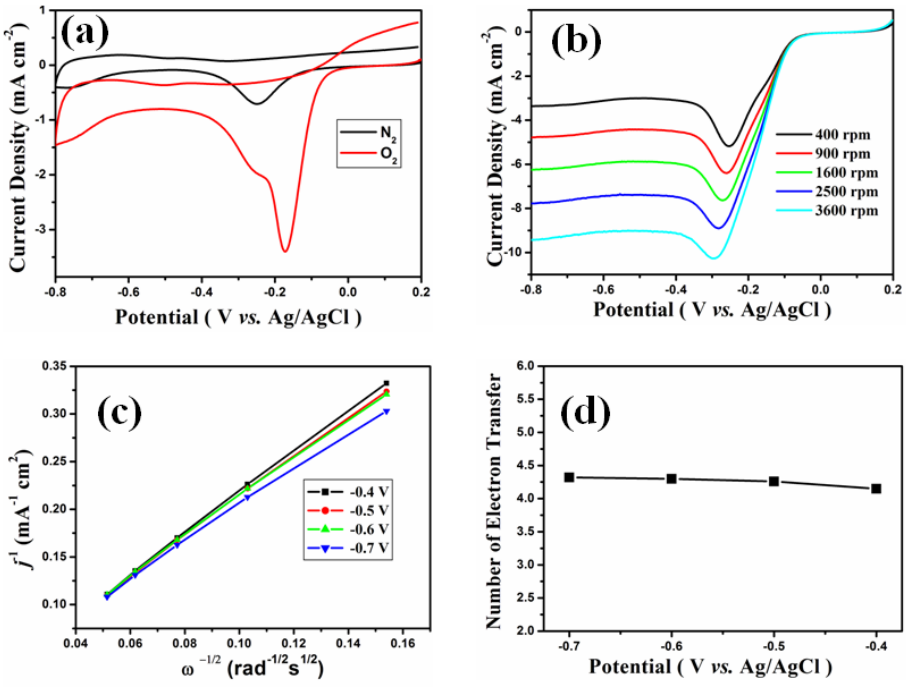

Figure 3.8: (a) CV plots of $Pd_3Fe_{0.5}Cu_{0.5}$/C, N_2- and O_2-saturated 0.1 M KOH solution with a scan rate of 50 mV s^{-1}, (b) Rotating rate-dependent ORR polarization curves for respective NPs with the scan rate of 10 mV s^{-1}, (c) K-L plots of j^{-1} *vs.* $\omega^{-1/2}$ for $Pd_3Fe_{0.5}Cu_{0.5}$/C NPs at different potential obtained from (b), and (d) The plot of the number of transferred electrons *vs.* potential for $Pd_3Fe_{0.5}Cu_{0.5}$/C NPs.

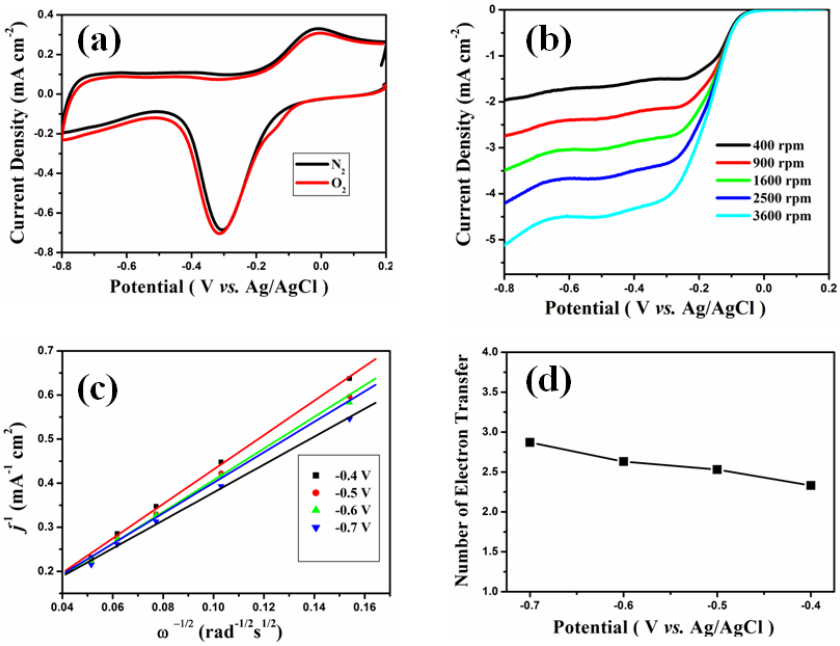

Figure 3.9: Electrochemical data for ORR over $PdFe_3$/C NPs. (a) CV plots in the N_2- and O_2-saturated 0.1 M KOH solution with a scan rate of 50 mV s^{-1}, (b) Rotating rate-dependent ORR polarization curves with the scan rate of 10 mVs^{-1}, (c) K–L plots of j^{-1} *vs.* $\omega^{-1/2}$ at different potential obtained from ORR results, and (d) The plot of the number of transferred electrons *vs.* potential.

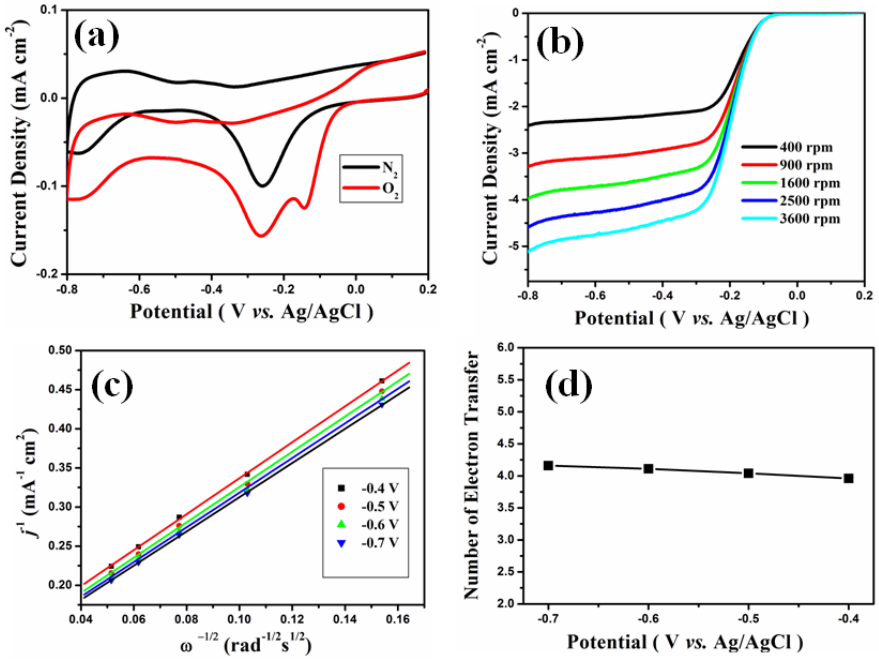

Figure 3.10: Electrochemical data for ORR over PdFe/C NPs. (a) CV plots in the N_2- and O_2-saturated 0.1 M KOH solution with a scan rate of 50 mV s^{-1}, (b) Rotating rate-dependent ORR polarization curves with the scan rate of 10 mV s^{-1}, (c) K–L plots of j^{-1} *vs.* $\omega^{-1/2}$ at different potential obtained from ORR results, and (d) The plot of the number of transferred electrons *vs.* potential.

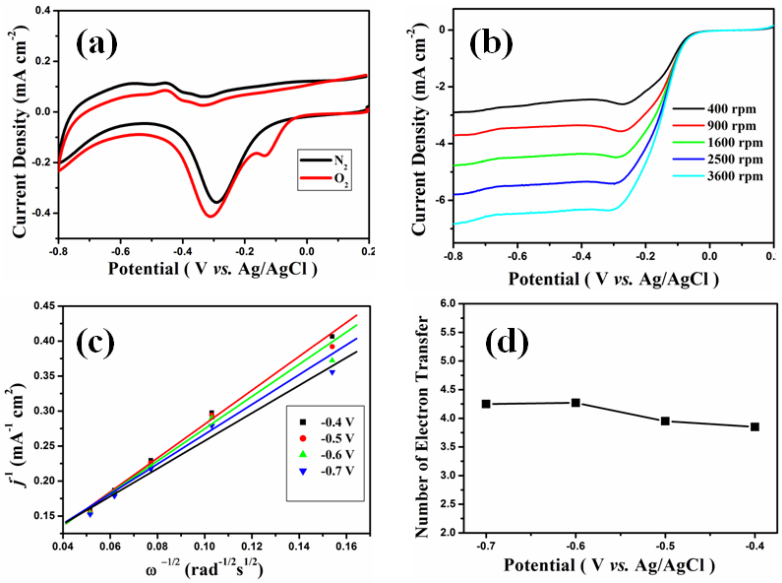

Figure 3.11: Electrochemical data for ORR over Pd_3Fe/C NPs. (a) CV plots in the N_2- and O_2-saturated 0.1 M KOH solution with a scan rate of 50 mV s^{-1}, (b) Rotating rate-dependent ORR polarization curves with the scan rate of 10 mV s^{-1}, (c) K–L plots of j^{-1} *vs.* $\omega^{-1/2}$ at different potential obtained from ORR results, and (d) The plot of the number of transferred electrons *vs.* potential.

The K–L plots obtained on the basis of the corresponding ORR polarization curves for $Pd_3Fe_{0.5}Cu_{0.5}$/C NPs at a potential of −0.40, −0.50, −0.60, and −0.70 V show good linearity (Figure 3.8c) thereby implying first-order kinetics for ORR. From the slope (1/B) of K–L plots, the n values for $Pd_3Fe_{0.5}Cu_{0.5}$/C NPs at −0.40, −0.50, −0.60, and −0.70 V can be calculated. Figure 3.8d gives the corresponding plot of 'n' *vs.* potential (V). It can be seen that the 'n' values from −0.40 to −0.70 V are ~4.0, suggesting that the ORR mechanism on $Pd_3Fe_{0.5}Cu_{0.5}$/C NPs follows the direct "4e^-" pathway ($O_2 + 2H_2O + 4e^- \rightarrow 4OH^-$). The electrocatalytic ORR mechanism of binary PdFe/C NPs also follow the direct "4e^-" pathway in the case of Pd_3Fe/C and PdFe/C NPs whereas "2e^-" pathway possibly in the case of $PdFe_3$/C NPs (Figures 3.9-3.11)

To elucidate the electrocatalytic behavior of the NPs, the electrochemically active surface area (ECSA) are calculated for all the NPs using CV curves in N_2-saturated 0.1 M KOH electrolyte at a scan rate 50 mV s^{-1} (Figure 3.12a). The peaks in the potential range −0.5 to 0 V originate from the palladium oxide reduction [42]. The ECSA of ternary $Pd_3Fe_{0.5}Cu_{0.5}$/C (63.22 m^2g^{-1}) is found to be higher than binary Pd_3Fe/C (32.99 m^2g^{-1}), PdFe/C (17.87 m^2g^{-1}), $PdFe_3$/C (8.3 m^2g^{-1}), standard Pt/C (8.7

m^2g^{-1}), and standard Pd/C (1.42 m^2g^{-1}). The improved electrocatalytic ORR activity can be co-related to the higher ECSA values. The higher ECSA values of the binary and ternary NPs can be attributed to the synergistic effect between the elements. To understand the superiority of the electrocatalytic performance, the ORR polarization curves for the standard Pd/C, standard Pt/C, binary $PdFe_3$/C, PdFe/C, Pd_3Fe/C and ternary $Pd_3Fe_{0.5}Cu_{0.5}$/C NPs are studied in O_2-saturated 0.1 M KOH electrolyte at a rotation of 1600 rpm and a scan rate of 10 mVs^{-1} (Figure 3.12b).

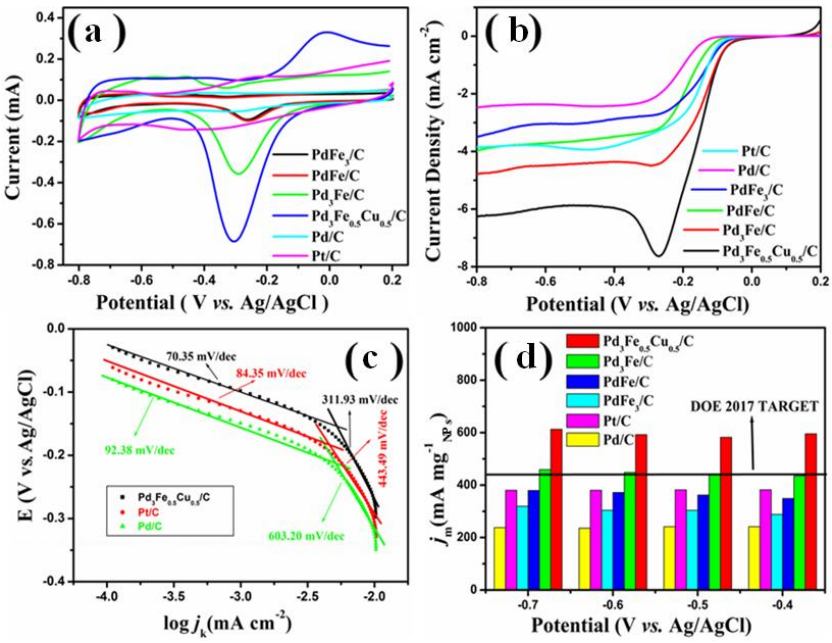

Figure. 3.12: (a) CV plots of all the electrocatalysts at N_2-saturated 0.1 M KOH solution at a scan rate of 50 mV s^{-1}, (b) Comparison of rotating rate-dependent ORR polarization curves for different catalyst at 1600 rpm, (c) Tafel plots, and (d) Mass activities of NPs under different potential at 1600 rpm. (These values are calculated as per the loading mass of the NPs).

The onset potential (E_{onset} = –0.044 V) and half-wave potential ($E_{1/2}$ = –0.145 V) of $Pd_3Fe_{0.5}Cu_{0.5}$/C NPs are found to be more positive than $Pd_3Fe_{0.5}Cu_{0.5}$/C NPs are found to be more positive than those of standard Pd/C (E_{onset} = –0.103 V, $E_{1/2}$ = –0.212 V), Pt/C (E_{onset} = –0.069 V, $E_{1/2}$ = –0.154 V), binary $PdFe_3$/C (E_{onset} = –0.047 V, $E_{1/2}$ = –0.168 V), PdFe/C (E_{onset} = –0.036 V, $E_{1/2}$ = –0.194 V), and Pd_3Fe/C (E_{onset} = –0.030 V, $E_{1/2}$ = –0.147 V) under identical conditions, suggesting superior ORR activity of the ternary $Pd_3Fe_{0.5}Cu_{0.5}$/C NPs. The overall ORR behavior follows the order:

$Pd_3Fe_{0.5}Cu_{0.5}/C$ > Pd_3Fe/C > PdFe/C > $PdFe_3/C$ > Pt/C > Pd/C. Moreover, the apparent current density values follow the same order.

To compare their electrocatalytic activities, the corresponding Tafel plots derived from the ORR polarization curves for all NPs are provided in Figure 3.12c and Figure 3.13. The Tafel slope calculated for $Pd_3Fe_{0.5}Cu_{0.5}/C$ in the high potential range (*i.e.*, –3.9 V to –2.5 V) is 70.35 mV dec^{-1}, while the other in the low potential range is 311.93 mV dec^{-1}. The two Tafel slopes indicate different ORR behaviors in different potential ranges [44]. These two slopes are comparatively smaller than those of standard Pt/C (84 and 443.4 mV dec^{-1}), Pd/C (92.38 and 603.2 mV dec^{-1}) as well as for other catalysts compositions and follows the order: Pd_3Fe/C (72 and 348.66 mV dec^{-1}) < PdFe/C (74.59 and 373.17 mV dec^{-1}) < $PdFe_3/C$ (78.92 and 393.74 mV dec^{-1}) < Pt/C (84 and 443.4 mV dec^{-1}) > Pd/C (92.38 and 603.2 mV dec^{-1}), in the high and low potential range, respectively.

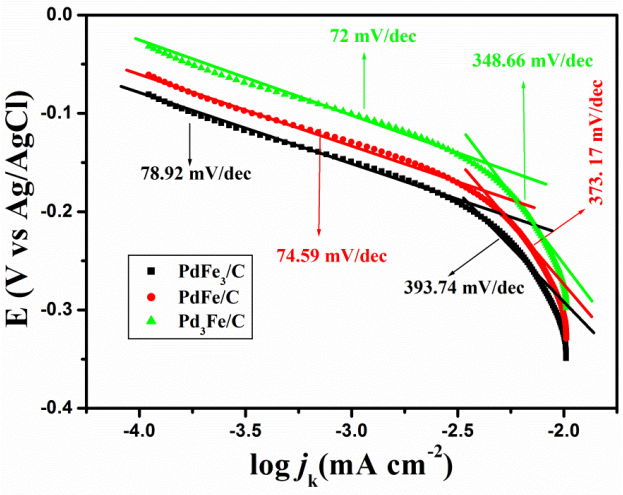

Figure 3.13: Comparison of Tafel plots Pd_3Fe/C, PdFe/C and $PdFe_3/C$ NPs.

This indicates that ternary $Pd_3Fe_{0.5}Cu_{0.5}/C$ has higher efficiency towards ORR as compared to that of the other catalyst systems studied and several reported Pd-based catalysts as detailed in Table 3.1. The mass activity (MA) and specific activity (SA) are the two important parameters for better assessment of the catalytic activity obtained by normalizing the kinetic current (j_k) w.r.t. the mass loading of the catalyst. Here, j_k has been calculated based on the K-L equation:

$$1/j = 1/j_k + 1/j_d$$

Where, j_k is the kinetic current, j_d is the diffusion limiting current and j is the current at a specific potential [44]. The mass activities of various NPs under different potential at 1600 rpm are presented in Figure 3.12d. The MA and SA of $Pd_3Fe_{0.5}Cu_{0.5}/C$ at –0.4 V (595.8 mA mg^{-1} and 84 mA cm^{-2}, respectively) are much higher than the Pt/C (382.2 mA mg^{-1} and 53.89 mA cm^{-2}) and Pd/C (241.6 mA mg^{-1} and 34.06 mA cm^{-2}) under the identical experimental conditions. The MA and SA values of $Pd_3Fe_{0.5}Cu_{0.5}/C$ are also larger than those of the PdFe/C NPs which follows the order: Pd_3Fe/C (434.9 mA mg^{-1} and 61.32 mA cm^{-2}) > PdFe/C (349 mA mg^{-1} and 49.20 mA cm^{-2}) > $PdFe_3/C$ (288.5 mA mg^{-1} and 40.67 mA cm^{-2}). These experimental findings are evident of the enriched kinetic ability of the $Pd_3Fe_{0.5}Cu_{0.5}/C$, making them an auspicious ORR catalyst.

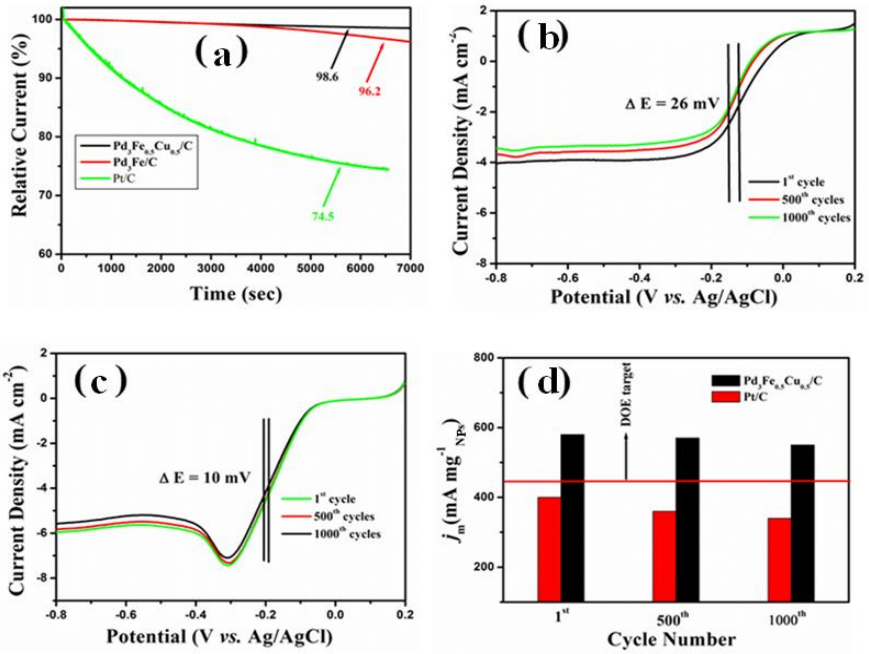

Figure 3.14: (a) CA curves of different catalysts, recorded at −0.3 V in a O_2-saturated 0.1 M KOH solution with a rotation rate of 1600 rpm towards ORR, (b) ORR polarization curves of Pt/C and (c) ORR polarization curves of $Pd_3Fe_{0.5}Cu_{0.5}/C$ at 1600 rpm before and after the stability test at different potential scans, (d) Comparison of mass activity after the stability test at different potential scans at 1600 rpm.

Apart from the activity, the high durability of the catalysts towards ORR is also an essential factor for energy conversion systems. Thus, to check the durability chronoamperometry (CA) test was performed in O_2-saturated 0.1 M KOH at –0.3V

(*vs.* Ag/AgCl) with a rotation speed of 1600 rpm for 7200 sec. It can be observed from Figure 3.14a that the initial activity decay for Pt/C and Pd_3Fe/C NPs are ~25.5% and ~3.8%, respectively after 7200 sec of testing, while the $Pd_3Fe_{0.5}Cu_{0.5}$/C NPs unveils only a loss of ~1.4% of its initial activity after 7200 sec, under identical experimental conditions. This demonstrates the excellent stability of the $Pd_3Fe_{0.5}Cu_{0.5}$/C NPs in basic media.

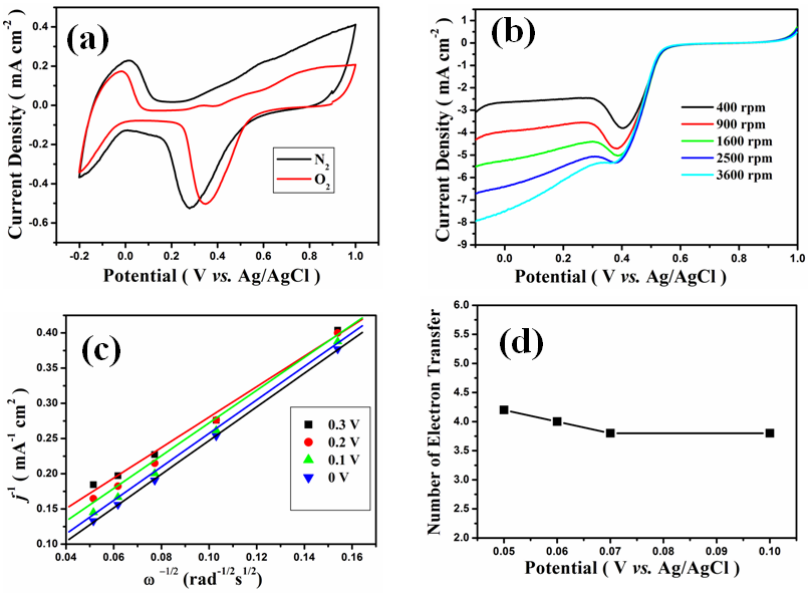

Figure 3.15: Electrochemical data for ORR over $Pd_3Fe_{0.5}Cu_{0.5}$/C NPs. (a) CV plots of $Pd_3Fe_{0.5}Cu_{0.5}$/C, N_2- and O_2-saturated 0.5 M H_2SO_4 solution with a scan rate of 50 mV s^{-1}, (b) Rotating rate-dependent ORR polarization curves for respective NPs with the scan rate of 10 mV s^{-1}, (c) K-L plots of j^{-1} *vs.* $\omega^{-1/2}$ for $Pd_3Fe_{0.5}Cu_{0.5}$/C NPs at different potential obtained from (b), and (d) The plot of the number of transferred electrons *vs.* potential for $Pd_3Fe_{0.5}Cu_{0.5}$/C NPs.

The structure and morphology of the $Pd_3Fe_{0.5}Cu_{0.5}$/C NPs as measured by TEM analyses after the CA test are shown in Figure 3.16. There is meager change in the morphology of the $Pd_3Fe_{0.5}Cu_{0.5}$/C NPs after the CA test. To support the structural stability, an accelerated durability test (ADT) is also performed for 1000 cycles between 0.2 V and –0.80 V *vs.* Ag/AgCl at a scan rate of 100 mV s^{-1} in O_2-saturated 0.1 M KOH solution for Pt/C and $Pd_3Fe_{0.5}Cu_{0.5}$/C NPs (Figure 3.14 b,c). Figure 3.14 b,c shows the associated ORR polarization curves at 1600 rpm before and after 500 and 1000 CV cycles. The MA of the $Pd_3Fe_{0.5}Cu_{0.5}$/C NPs has been deteriorated to a lower extent (5.17%) in comparison to Pt/C (11%) after 1000 potential CV cycles.

There is a clear drop of onset potential in the case of Pt/C, whereas, the onset potential remains almost same after 500 and 1000 cycles for $Pd_3Fe_{0.5}Cu_{0.5}$/C catalyst. The $E_{1/2}$ of Pt/C (26 mV) also shows a larger change compared to that of $Pd_3Fe_{0.5}Cu_{0.5}$/C (10 mV) NPs. The above discussion indicates that $Pd_3Fe_{0.5}Cu_{0.5}$/C NPs is the most efficient catalyst in basic media. To generalize the ORR behavior of the $Pd_3Fe_{0.5}Cu_{0.5}$/C NPs in the acidic electrolyte, we conducted electrocatalytic studies in 0.5 M H_2SO_4 solution. As presented in Figure 3.15, it is apparent that $Pd_3Fe_{0.5}Cu_{0.5}$/C NPs is very active towards ORR in 0.5 M H_2SO_4 solution as well. It can be seen that the 'n' values from 0.1 to 0.05 V are ~4.0, suggesting that the ORR mechanism on $Pd_3Fe_{0.5}Cu_{0.5}$/C NPs follows the direct "$4e^-$" pathway ($O_2 + 4H^+ + 4e^- \rightarrow 2H_2O$).

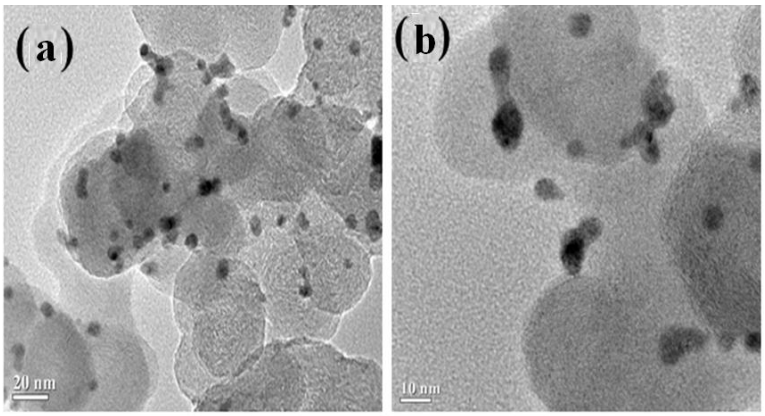

Figure 3.16: TEM and HR-TEM images of $Pd_3Fe_{0.5}Cu_{0.5}$/C after CA test.

The enhanced ORR performance of $Pd_3Fe_{0.5}Cu_{0.5}$/C NPs is due to their unique structural and compositional superiorities. From the HR-TEM images, the unique half-embedded and half-exposed interface structure was seen. i.e., one-half of NPs are embedded into the carbon matrix and another part is exposed from the carbon matrix. Therefore, there is a stable electronic coupling between the carbon matrix and $Pd_3Fe_{0.5}Cu_{0.5}$ NPs. This means that the half-embedded part possess very faster interfacial electron transfer ultimately enhancing the conductivity of the $Pd_3Fe_{0.5}Cu_{0.5}$ NPs. Moreover the other exposed part is also highly active as the reactant molecule (O_2 diffusion layer) directly interacts with the catalyst layer. The carbon matrix also acts as superior support as they effectively prevent the NPs aggregation, improving the stability of the $Pd_3Fe_{0.5}Cu_{0.5}$ in the electrochemical process. Furthermore, $Pd_3Fe_{0.5}Cu_{0.5}$/C NPs exhibit many crystal defects on their surfaces, including vacancy,

atomic steps and dislocation defects, that can work as abundant catalytically active sites accessible to the reactant, ultimately enhancing ORR activity.

Alloying Pd (fully occupied d-orbital) with Fe and Cu (low occupancy d-orbital) can improve the electronic properties of Pd, which ultimately enhance the electro catalytic activity [13,45–48] by decreasing the Gibbs free energy of the electronic transition involved in the ORR process [49,50]. One of the salient parameters to understand the enhancement of ORR activity is the lattice strain effect in catalysts. The lattice strain changes the d-band center of the metal catalyst, which resolve the surface oxygen adsorption property of the catalyst surface [51–53]. A down shift in the d-band center of Pd weakens the binding energy of absorption of intermediates such as OH^-_{ads} and CO_{ads} thereby conserves more active sites on the catalyst surface. As a result, the catalyst shows better electrocatalytic activity [54]. In 2000, Norskov *et al*. proposed that the lattice strain in Pd lattice in PdFe alloy lowers the d-band centers by −0.88 eV using DFT calculation [55]. Incorporation of Cu and Fe with small lattice parameters in Pd (0.38898 nm) with large lattice parameter result in lattice strain in Pd alloys. In this case, we have calculated lattice strain from XRD data that $Pd_3Fe_{0.5}Cu_{0.5}/C$ has the smallest lattice parameter among all the PdFe/C NPs, Pd/C and Pt/C.

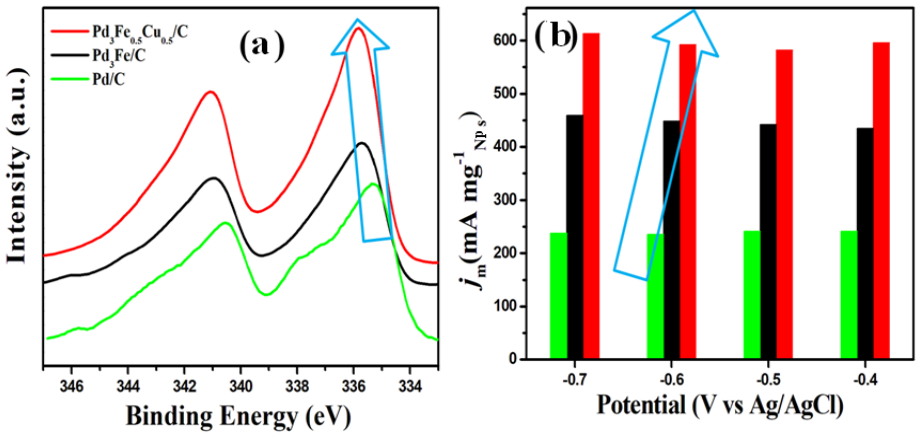

Figure 3.17: Correlation of binding energy change of Pd 3d to ORR activity in terms of mass activity for $Pd_3Fe_{0.5}Cu_{0.5}/C$ (red), Pd_3Fe/C (black), and Pd/C (green) NPs.

One of the most important parameters for high performance ORR activity is the linear relation between the metal d-band center (ε_d, with respect to Fermi level) and binding energy of adsorbed species on the metal surface (e.g., oxygen, hydrogen and methanol) [15]. For oxygen adsorption, an upper weight position in ε_d increases the

interaction of the 2p states oxygen with the metal d states, i.e., forms a stronger metal-oxygen bond. On the other hand, a downshift of ε_d causes a weak interaction with oxygen [19, 56–59]. The positive shifts of binding energy represent a downshift of d-band center with respect to Fermi level. The downshift of Pd d-band center can further be closely correlated with the weaker Pd-O bond energy, by means of which the intermediate OH_{ad} species adsorption on the Pd surface can be decreased,[15, 58, 60–62] thus sustaining the more active sites for ORR and at the end resulting in the enrichment in ORR activity [18, 58, 63, 64]. For that reason, the alteration of the d band center for Pt or Pd through the formation of alloys with second metals could increase the kinetics of the ORR. There are several theoretical reports on ORR where DFT calculation has been used over various catalyst alloys with compositions of Pt_3X or Pd_3X (X = Cu, Ni, Co, Fe, Ag, Au, Ir, etc.) by using d-band center model [15, 58]. The upshift of ~0.50 and ~0.40 eV in the binding energies of Pd $3d_{5/2}$ for $Pd_3Fe_{0.5}Cu_{0.5}$/C and Pd_3Fe/C NPs in comparison to Pd/C as shown is Figure 3.17 implies the aforesaid down shift trends of Pd d-band center which leads to the enhancement of the catalytic performance and acceleration in terms of mass activity of the ORR activity. Thus, among all the catalytic systems, the $Pd_3Fe_{0.5}Cu_{0.5}$/C shows the best electrocatalytic activity towards ORR in both acidic and basic media.

Table 3.1: Comparison of the ORR performance parameters of $Pd_3Fe_{0.5}Cu_{0.5}$/C with recently reported some seminal works of Pd-based electrocatalysts in 0.1 M KOH solution.

Sl. No.	Catalysts	Tafel Slope (mV dec^{-1})	E_0 V (*vs.* Ag/AgCl)	$E_{1/2}$ V (*vs.* Ag/AgCl)	References
1.	Pd-g-C_3N_4	--	-0.0653	–	65
2.	G-$FePd_3$	--	-0.0403	–	66
3.	G-Cu_3Pd	68.9	-0.0133	–	67
4.	PdCo/NPC	--	-0.00373	-0.1223	68
5.	Pd_3Pb/C	--	0.0647	-0.0453	69
6.	Pd_3Fe/C	71.4	0.0847	–	70
7.	Pd_3Pb	56.3	--	-0.9522	71
8.	PdCuNi	--	–	-0.1033	72
9.	PdCuCo	--		-0.0933	
10.	Pd_2NiAg	--	-0.0423	-0.1233	73
11.	Pt@PdNFs/rGO	--	-0.0553	-0.1453	74

12.	AuPdCo/C	--	0.0347	−	75
13.	$MnPd_3$/C	65	-0.0123	-0.1653	76
14.	PdNiCu/NG	--	−	-0.2023	77
15.	PdNiSn/NG	--			
16.	**$Pd_3Fe_{0.5}Cu_{0.5}$/C**	**70.35**	**0.044 V**	**-0.145**	**This work**

3.2. Conclusions

In summary, we have adopted a facile synthesis of various compositions of PdFe/C and $Pd_3Fe_{0.5}Cu_{0.5}$/C nanoalloys that exhibited remarkably enhanced catalytic activity towards ORR. The Cu incorporated Pd_3Fe/C NPs modified the lattice constrain and d-band center of the $Pd_3Fe_{0.5}Cu_{0.5}$/C, which impressively displayed superior activity and long term stability when used as a cathode electrocatalyst. The nanoalloy with defects on their surfaces, for instance; vacancy, dislocation and low-coordinate atomic steps offer numerous energetic sites accessible to catalyze the fuel cell reaction. Therefore, the present investigation offers new possibilities for the development of sustainable energy conversion and related technologies with superior activity, favorable kinetics and long term durability in relatively low cost.

References

[1] Nie, Y., Li, L., and Wei, Z. Recent advancements in Pt and Pt-free catalysts for oxygen reduction reaction. *Chemical Society Reviews*, 44(8):2168−2201, 2015.

[2] Zhang, Z., More, K. L., Sun, K., Wu, Z., and Li, W. Preparation and characterization of PdFe nanoleaves as electrocatalysts for oxygen reduction reaction. *Chemistry of Materials*, 23(6):1570−1577, 2011.

[3] Son, D. N., and Takahashi, K. Selectivity of palladium–cobalt surface alloy toward oxygen reduction reaction. *The Journal of Physical Chemistry C*, 116(10):6200−6207, 2012.

[4] Li, W., and Haldar, P. Supportless PdFe nanorods as highly active electrocatalyst for proton exchange membrane fuel cell. *Electrochemistry Communications*, 11(6):1195−1198, 2009.

[5] Han, B., and Xu, C. Nanoporous PdFe alloy as highly active and durable electrocatalyst for oxygen reduction reaction. *International Journal of Hydrogen Energy*, 39(32):18247−18255, 2014.

[6] Kang, Y. S., Choi, K.-H., Ahn, D., Lee, M. J., Baik, J., Chung, D. Y., Kim, M.-J., Lee, S. Y., Kim, M., Shin, H., Lee, K.-S., and Sung, Y.-E. Effect of post heat-treatment of composition-controlled PdFe nanoparticles for oxygen reduction reaction. *Journal of Power Sources*, 303: 234-242, 2016.

[7] Yang, L., Hu, C., Wang, J., Yang, Z., Guo, Y., Bai, Z., and Wang, K. Facile synthesis of hollow palladium/copper alloyed nanocubes for formic acid oxidation. *Chemical Communications*, 47(30):8581−8583, 2011.

[8] Li, J., Zhou, H., Zhuo, H., Wei, Z., Zhuang, G., Zhong, X., Deng, S., Li, X., and Wang, J. Oxygen vacancies on TiO_2 promoted the activity and stability of supported Pd nanoparticles for the oxygen reduction reaction. *Journal of Materials Chemistry A*, 6(5):2264−2272, 2018.

[9] Heemeier, M., Carlsson, A. F., Naschitzki, M., Schmal, M., Bäumer, M., and Freund, H.-J. Preparation and characterization of a model bimetallic catalyst: Co–Pd nanoparticles supported on Al_2O_3. *Angewandte Chemie International Edition*, 41(21):4073−4076, 2002.

[10] Wang, M., Qin, X., Jiang, K., Dong, Y., Shao, M., and Cai, W. -B. Electrocatalytic Activities of Oxygen Reduction Reaction on Pd/C and Pd-B/C Catalysts. *Journal of Physical Chemistry C*, 121(6):3416−3423, 2017.

[11] Dutta, A., and Datta, J. Outstanding catalyst performance of PdAuNi nanoparticles for the anodic reaction in an alkaline direct ethanol (with anion-exchange membrane) fuel cell. *The Journal of Physical Chemistry C*, 116(49):25677−25688, 2012.

[12] Chen, Z., He, Y.-C., Chen, J.-H., Fu, X.-Z., Sun, R., Chen, Y.-X., and Wong, C.-P. PdCu alloy flower-like nanocages with high electrocatalytic performance for methanol oxidation. *The Journal of Physical Chemistry C*, 122(16):8976−8983, 2018.

[13] Mazumder, V., Chi, M., Mankin, M. N., Liu, Y., Metin, Ö., Sun, D., More, K. L., and Sun, S. A facile synthesis of MPd (M = Co, Cu) nanoparticles and their catalysis for formic acid oxidation. *Nano Letters*, 12(2):1102−1106, 2012.

[14] Shao, M. H., Sasaki, K., and Adzic, R. R. Pd−Fe nanoparticles as electrocatalysts for oxygen reduction. *Journal of the American Chemical Society*, 128(11):3526−3527, 2006.

[15] Shao, M., Liu, P., Zhang, J., and Adzic, R. Origin of enhanced activity in

palladium alloy electrocatalysts for oxygen reduction reaction. *The Journal of Physical Chemistry B*, 111(24):6772−6775, 2007.

[16] Cho, Y. H., Kim, O. H., Chung, D. Y., Choe, H., Cho, Y. H., and Sung, Y. E. PtPdCo ternary electrocatalyst for methanol tolerant oxygen reduction reaction in direct methanol fuel cell. *Applied Catalysis B: Environmental*, 154:309−315, 2014.

[17] Negro, E., Vezzù, K., Bertasi, F., Schiavuta, P., Toniolo, L., Polizzi, S., and Di Noto, V. Interplay between nitrogen concentration, structure, morphology, and electrochemical performance of PdCoNi "core-shell" carbon nitride electrocatalysts for the oxygen reduction reaction. *ChemElectroChem*, 1(8):1359−1369, 2014.

[18] Luo, L., Zhu, F., Tian, R., Li, L., Shen, S., Yan, X., and Zhang, J. Composition-graded Pd_xNi_{1-x} nanospheres with Pt monolayer shells as high-performance electrocatalysts for oxygen reduction reaction. *ACS Catalysis*, 7(8):5420−5430, 2017.

[19] Lin, F., Wang, K., Tang, Y., Lai, J., Lou, M., Huang, M., and Guo, S. Enhanced bifunctional fuel cell catalysis *via* Pd/PtCu core/shell nanoplates. *Chemical Communications*, 54(11):1315−1318, 2018.

[20] Fernández, J. L., Raghuveer, V., Manthiram, A., and Bard, A. J. Pd−Ti and Pd−Co−Au electrocatalysts as a replacement for platinum for oxygen reduction in proton exchange membrane fuel cells. *Journal of the American Chemical Society*, 127(38):13100−13101, 2005.

[21] Liu, Y., Liu, S., Che, Z., Zhao, S., Sheng, X., Han, M., and Bao, J. Concave octahedral Pd@PdPt electrocatalysts integrating core–shell, alloy and concave structures for high-efficiency oxygen reduction and hydrogen evolution reactions. *Journal of Materials Chemistry A*, 4(42):16690−16697, 2016.

[22] Yeh, Y.-C., Chen, H. M., Liu, R.-S., Asakura, K., Lo, M.-Y., Peng, Y.-M., Chan, T.-S., and Lee, J.-F. Pd−C−Fe nanoparticles investigated by X-ray absorption spectroscopy as electrocatalysts for oxygen reduction. *Chemistry of Materials*, 21(17):4030−4036, 2009.

[23] Boone, C. V., and Maia, G. Pt–Pd and Pt–Pd–(Cu or Fe or Co)/graphene nanoribbon nanocomposites as efficient catalysts toward the oxygen reduction reaction. *Electrochimica Acta*, 247:19−29, 2017.

[24] Wang, F., Li, C., Sun, L.-D., Xu, C.-H., Wang, J., Yu, J. C., and Yan, C.-H. Porous single-crystalline palladium nanoparticles with high catalytic activities. *Angewandte Chemie International Edition*, 51(20):4872−4876, 2012.

[25] Wang, L., and Yamauchi, Y. Block copolymer mediated synthesis of dendritic platinum nanoparticles. *Journal of the American Chemical Society*, 131(26):9152−9153, 2009.

[26] Yin, A.-X., Min, X.-Q., Zhu, W., Wu, H.-S., Zhang, Y.-W., and Yan, C.-H. Multiply twinned Pt–Pd nanoicosahedrons as highly active electrocatalysts for methanol oxidation. *Chemical Communications*, 48(4):543−545, 2012.

[27] Zhang, C., Zhang, J., Han, B., Zhao, Y., and Li, W. Synthesis of icosahedral gold particles by a simple and mild route. *Green Chemistry*, 10(10):1094−1098 2008.

[28] Du, J., Chen, C., Cheng, F., and Chen, J. Rapid synthesis and efficient electrocatalytic oxygen reduction/evolution reaction of $CoMn_2O_4$ nanodots supported on graphene. *Inorganic Chemistry*, 54(11):5467−5474, 2015.

[29] Lu, Y., Zhao, S., Yang, R., Xu, D., Yang, J., Lin, Y., Shi, N.-E., Dai, Z., Bao, J., and Han, M. Well-coupled nanohybrids obtained by component-controlled synthesis and in situ integration of Mn_xPd_y nanocrystals on vulcan carbon for electrocatalytic oxygen reduction. *ACS Applied Materials & Interfaces*, 10(9):8155−8164, 2018.

[30] Chai, J., Li, F., Hu, Y., Zhang, Q., Han, D., and Niu, L. Hollow flower-like AuPd alloy nanoparticles: One step synthesis, self-assembly on ionic liquid-functionalized graphene, and electrooxidation of formic acid. *Journal of Materials Chemistry*, 21(44): 17922−17929, 2011.

[31] Ghosh, S., Bhandary, N., Basu, S., and Basu, R. N. Synergistic effects of polypyrrole nanofibers and Pd nanoparticles for improved electrocatalytic performance of Pd/PPy nanocomposites for ethanol oxidation. *Electrocatalysis*, 8(4):329−339, 2017.

[32] Yamashita, T., and Hayes, P. Analysis of XPS spectra of Fe^{2+} and Fe^{3+} ions in oxide materials. *Applied Surface Science*, 254(8):2441−2449, 2008.

[33] Kokate, M., Dapurkar, S., Garadkar, K., and Gole, A. Magnetite–silica–gold nanocomposite: one-pot single-step synthesis and its application for solvent-free oxidation of benzyl alcohol. *The Journal of Physical Chemistry C*,

119(25):14214−14223, 2015.

[34] Gole, A., Stone, J. W., Gemmill, W. R., zur Loye, H.-C., and Murphy, C. J. Iron oxide coated gold nanorods: synthesis, characterization, and magnetic manipulation. *Langmuir*, 24(12):6232−6237, 2008.

[35] Sun, Y., Duan, L., Guo, Z., DuanMu, Y., Ma, M., Xu, L., Zhang, Y., and Gu, N. An improved way to prepare superparamagnetic magnetite-silica core-shell nanoparticles for possible biological application. *Journal of Magnetism and Magnetic Materials*, 285(1-2):65−70, 2005.

[36] Teng, X., Black, D., Watkins, N. J., Gao, Y., and Yang, H. Platinum-maghemite core−shell nanoparticles using a sequential synthesis. *Nano Letters*, 3(2):261−264, 2003.

[37] Li, F., Li, J., Lin, X., Li, X., Fang, Y., Jiao, L., An, X., Fu, Y., Jin, J., and Li, R. Designed synthesis of multi-walled carbon nanotubes@Cu@MoS_2 hybrid as advanced electrocatalyst for highly efficient hydrogen evolution reaction. *Journal of Power Sources*, 300:301−308, 2015.

[38] Jin, Z., Liu, C., Qi, K., and Cui, X. Photo-reduced Cu/CuO nanoclusters on TiO_2 nanotube arrays as highly efficient and reusable catalyst. *Scientific Reports*, 7(1):39695, 2017.

[39] Ghosh, A., Chandran, P., and Ramaprabhu, S. Palladium-nitrogen coordinated cobalt alloy towards hydrogen oxidation and oxygen reduction reactions with high catalytic activity in renewable energy generations of proton exchange membrane fuel cell. *Applied Energy*, 208:37−48, 2017.

[40] Çelik, B., Yıldız, Y., Sert, H., Erken, E., Koşkun, Y., and Şen, F. Monodispersed palladium–cobalt alloy nanoparticles assembled on poly(N-vinyl-pyrrolidone) (PVP) as a highly effective catalyst for dimethylamine borane (DMAB) dehydrocoupling. *RSC Advances*, 6(29):24097−24102, 2016.

[41] Komatsu, T., and Tamura, A. Pt_3Co and PtCu intermetallic compounds: Promising catalysts for preferential oxidation of CO in excess hydrogen. *Journal of Catalysis*, 258(2):306−314, 2008.

[42] Dehghani Sanij, F., and Gharibi, H. Preparation of bimetallic alloyed palladium-nickel electro-catalysts supported on carbon with superior catalytic performance towards oxygen reduction reaction. *Colloids and Surfaces A: Physicochemical and Engineering Aspects*, 538:429−442, 2018.

[43] Parvez, K., Yang, S., Hernandez, Y., Winter, A., Turchanin, A., Feng, X., and Müllen, K. Nitrogen-doped graphene and its iron-based composite as efficient electrocatalysts for oxygen reduction reaction. *ACS Nano*, 6(11):9541−9550, 2012.

[44] Shi, Q., Zhu, C., Bi, C., Xia, H., Engelhard, M. H., Du, D., and Lin, Y. Intermetallic Pd_3Pb nanowire networks boost ethanol oxidation and oxygen reduction reactions with significantly improved methanol tolerance. *Journal of Materials Chemistry A*, 5(45):23952−23959, 2017.

[45] Chen, D., Sun, P., Liu, H., and Yang, J. Bimetallic Cu–Pd alloy multipods and their highly electrocatalytic performance for formic acid oxidation and oxygen reduction. *Journal of Materials Chemistry A*, 5(9):4421−4429, 2017.

[46] Zhang, Z., Liu, S., Tian, X., Wang, J., Xu, P., Xiao, F., and Wang, S. Facile synthesis of N-doped porous carbon encapsulated bimetallic PdCo as a highly active and durable electrocatalyst for oxygen reduction and ethanol oxidation. *Journal of Materials Chemistry A*, 5(22):10876−10884, 2017.

[47] Wang, D., Xin, H. L., Yu, Y., Wang, H., Rus, E., Muller, D. A., and Abruña, H. D. Pt-decorated PdCo@Pd/C core−shell nanoparticles with enhanced stability and electrocatalytic activity for the oxygen reduction reaction. *Journal of the American Chemical Society*, 132(50):17664−17666, 2010.

[48] Liu, D., Guo, Q., Hou, H., Niwa, O., and You, T. Pd_xCo_y nanoparticle/carbon nanofiber composites with enhanced electrocatalytic properties. *ACS Catalysis*, 4(6):1825−1829, 2014.

[49] Xue, H., Tang, J., Gong, H., Guo, H., Fan, X., Wang, T., He, J., and Yamauchi, Y. Fabrication of PdCo bimetallic nanoparticles anchored on three-dimensional ordered N-doped porous carbon as an efficient catalyst for oxygen reduction reaction. *ACS Applied Materials & Interfaces*, 8(32):20766−20771, 2016.

[50] Wang, Y. and Balbuena, P. B. Design of oxygen reduction bimetallic catalysts: ab-initio-derived thermodynamic guidelines. *The Journal of Physical Chemistry B*, 109(40):18902−18906, 2005.

[51] Xiao, W., Cordeiro, M. A. L., Gong, M., Han, L., Wang, J., Bian, C., Zhu, J., Xin, H. L., and Wang, D. Optimizing the ORR activity of Pd based nanocatalysts by tuning their strain and particle size. *Journal of Materials Chemistry A*, 5(20):9867−9872, 2017.

[52] Kibler, L. A., El-Aziz, A. M., Hoyer, R., and Kolb, D. M. Tuning reaction rates by lateral strain in a palladium monolayer. *Angewandte Chemie International Edition*, 44(14):2080−2084, 2005.

[53] Kumar, S. and Zou, S. Electrooxidation of carbon monoxide and methanol on platinum-overlayer-coated gold nanoparticles: effects of film thickness. *Langmuir*, 23(13):7365−7371, 2007.

[54] Wang, Q., Zhao, Q., Su, Y., Zhang, G., Xu, G., Li, Y., Liu, B., Zheng, D., and Zhang, J. Hierarchical carbon and nitrogen adsorbed PtNiCo nanocomposites with multiple active sites for oxygen reduction and methanol oxidation reactions. *Journal of Materials Chemistry A*, 4(31):12296−12307, 2016.

[55] Hammer, B., and Nørskov, J. K. Theoretical surface science and catalysis—calculations and concepts. In: *Advances in Catalysis*. 45:71−129, 2000.

[56] Stamenkovic, V., Mun, B. S., Mayrhofer, K. J. J., Ross, P. N., Markovic, N. M., Rossmeisl, J., Greeley, J., and Nørskov, J. K. Changing the activity of electrocatalysts for oxygen reduction by tuning the surface electronic structure. *Angewandte Chemie International Edition*, 118(18):2963−2967, 2006.

[57] Stamenkovic, V. R., Mun, B. S., Arenz, M., Mayrhofer, K. J. J., Lucas, C. A., Wang, G., Ross, P. N., and Markovic, N. M. Trends in electrocatalysis on extended and nanoscale Pt-bimetallic alloy surfaces. *Nature Materials*, 6(3):241−247, 2007.

[58] Greeley, J., Stephens, I. E. L., Bondarenko, A. S., Johansson, T. P., Hansen, H. A., Jaramillo, T. F., Rossmeisl, J., Chorkendorff, I., and Nørskov, J. K. Alloys of platinum and early transition metals as oxygen reduction electrocatalysts. *Nature Chemistry*, 1(7):552−556, 2009.

[59] Henry, J. B., Maljusch, A., Huang, M., Schuhmann, W., and Bondarenko, A. S. Thin-film Cu–Pt(111) near-surface alloys: active electrocatalysts for the oxygen reduction reaction. *ACS Catalysis*, 2(7):1457−1460, 2012.

[60] Seo, M. H., Choi, S. M., Lee, D. U., Kim, W. B., and Chen, Z. Correlation between theoretical descriptor and catalytic oxygen reduction activity of graphene supported palladium and palladium alloy electrocatalysts. *Journal of Power Sources*, 300:1−9, 2015.

[61] Hammer, B., and Norskov, J. K. Why gold is the noblest of all the metals. *Nature*, 376(6537):238−240, 1995.

[62] Shao, M., K. Sasaki, Marinkovic, N., Zhang, L., and Adzic, R. Synthesis and characterization of platinum monolayer oxygen-reduction electrocatalysts with Co–Pd core–shell nanoparticle supports. *Electrochemistry Communications*, 9(12):2848−2853, 2007.

[63] Shao, M. H., Huang, T., Liu, P., Zhang, J., Sasaki, K., Vukmirovic, M. B., and Adzic, R. R. Palladium monolayer and palladium alloy electrocatalysts for oxygen reduction. *Langmuir*, 22(25):10409−10415, 2006.

[64] Koenigsmann, C., Santulli, A. C., Gong, K., Vukmirovic, M. B., Zhou, W., Sutter, E., Wong, S. S., and Adzic, R. R. Enhanced electrocatalytic performance of processed, ultrathin, supported Pd–Pt core–shell nanowire catalysts for the oxygen reduction reaction. *Journal of the American Chemical Society*, 133(25):9783−9795, 2011.

[65] Konda, S. K., Amiri, M., and Chen, A. Photoassisted deposition of palladium nanoparticles on carbon nitride for efficient oxygen reduction. *The Journal of Physical Chemistry C*, 120(27):14467−14473, 2016.

[66] Yin, H., Liu, S., Zhang, C., Bao, J., Zheng, Y., Han, M., and Dai, Z. Well-coupled graphene and Pd-based bimetallic nanocrystals nanocomposites for electrocatalytic oxygen reduction reaction. *ACS Applied Materials & Interfaces*, 6(3):2086−2094, 2014.

[67] Zheng, Y., Zhao, S., Liu, S., Yin, H., Chen, Y.-Y., Bao, J., Han, M., and Dai, Z. Component-controlled synthesis and assembly of Cu–Pd nanocrystals on graphene for oxygen reduction reaction. *ACS Applied Materials & Interfaces*, 7(9):5347−5357, 2015.

[68] Xue, H., Tang, J., Gong, H., Guo, H., Fan, X., Wang, T., He, J., and Yamauchi, Y. Fabrication of PdCo bimetallic nanoparticles anchored on three-dimensional ordered N-doped porous carbon as an efficient catalyst for oxygen reduction reaction. *ACS Applied Materials & Interfaces*, 8(32):20766−20771, 2016.

[69] Cui, Z., Chen, H., Zhao, M., and DiSalvo, F. J. High-performance Pd_3Pb intermetallic catalyst for electrochemical oxygen reduction. *Nano Letters*, 16(4):2560−2566, 2016.

[70] Cui, Z., Li, L., Manthiram, A., and Goodenough, J. B. Enhanced cycling stability of hybrid Li–air batteries enabled by ordered Pd_3Fe intermetallic electrocatalyst. *Journal of the American Chemical Society*, 137(23):7278−7281,

2015.

[71] Shi, Q., Zhu, C., Bi, C., Xia, H., Engelhard, M. H., Du, D., and Lin, Y. Intermetallic Pd_3Pb nanowire networks boost ethanol oxidation and oxygen reduction reactions with significantly improved methanol tolerance. *Journal of Materials Chemistry A*, 5(45):23952−23959, 2017.

[72] Jiang, K., Wang, P., Guo, S., Zhang, X., Shen, X., Lu, G., Su, D., and Huang, X. Ordered PdCu-based nanoparticles as bifunctional oxygen-reduction and ethanol-oxidation electrocatalysts. *Angewandte Chemie International Edition*, 55(31):9030−9035, 2016.

[73] Liu, S., Zhang, Q., Li, Y., Han, M., Gu, L., Nan, C., Bao, J., and Dai, Z. Five-fold twinned Pd_2NiAg nanocrystals with increased surface ni site availability to improve oxygen reduction activity. *Journal of the American Chemical Society*, 137(8):2820−2823, 2015.

[74] Lin, X.-X., Wang, A.-J., Fang, K.-M., Yuan, J., and Feng, J.-J. One-pot seedless aqueous synthesis of reduced graphene oxide (rGO)-supported core–shell Pt@Pd nanoflowers as advanced catalysts for oxygen reduction and hydrogen evolution. *ACS Sustainable Chemistry & Engineering*, 5(10):8675−8683, 2017.

[75] Kuttiyiel, K. A., Sasaki, K., Su, D., Wu, L., Zhu, Y., and Adzic, R. R. Gold-promoted structurally ordered intermetallic palladium cobalt nanoparticles for the oxygen reduction reaction. *Nature Communications*, 5(1):5185, 2014.

[76] Lu, Y., Zhao, S., Yang, R., Xu, D., Yang, J., Lin, Y., Shi, N.-E., Dai, Z., Bao, J., and Han, M. Well-coupled nanohybrids obtained by component-controlled synthesis and in situ integration of Mn_xPd_y nanocrystals on vulcan carbon for electrocatalytic oxygen reduction. *ACS Applied Materials & Interfaces*, 10(9):8155−8164, 2018.

[77] Sun, L., Liao, B., Ren, X., Li, Y., Zhang, P., Deng, L., and Gao, Y. Ternary PdNi-based nanocrystals supported on nitrogen-doped reduced graphene oxide as highly active electrocatalysts for the oxygen reduction reaction. *Electrochimica Acta*, 235:543−552, 2017.